Electronic Supplementary Information

Experimental section

Materials: Ti_2O_3 (100 mesh, 99.9%) was purchased from Sigma-Aldrich. Hydrochloric acid (HCl, 36.0-38.0%), ammonium chloride (NH_4Cl, 99.5%), sodium hypochlorite (NaClO, AR), sodium hydroxide (NaOH, AR), salicylic acid ($C_7H_6O_3$, AR), sodium citrate dihydrate ($C_6H_5Na_3O_7 \cdot 2H_2O$, AR), sodium nitroferricyanide (III) dihydrate ($Na_2Fe(CN)_5NO \cdot 2H_2O$, 99.0%), para-(dimethylamino) benzaldehyde ($C_9H_{11}NO$, 99.0%), and Nafion solution (5 wt%) were purchased from Aladdin Reagent Co., Ltd. Absolute ethanol (C_2H_5OH, 99.7%) and hydrazine hydrate ($N_2H_4 \cdot H_2O$, AR) were purchased from Beijing Chemical Corporation. Carbon paper was bought from Taiwan CeTech Company. The deionized water used throughout all experiments was purified by a Millipore system. All reagents were analytical reagent grade without further purification.

Preparation of OV-Ti_2O_3: Plasma treatment was performed on an AX-1000II plasma system with a radio frequency power generator (13.56 MHz) at room temperature. Ti_2O_3 particles were treated by Ar plasma for 300 s at a radiofrequency power of 600 W and a pressure of 20 Pa in Ar atmosphere (20 sccm) to obtain OV-Ti_2O_3.

Preparation of OV-Ti_2O_3/CP and pristine Ti_2O_3/CP: Typically, 10 mg of catalyst and 40 μL of the 5 wt% Nafion solution were dispersed in 720 μL of absolute ethanol and 240 μL of deionized water and ultrasonicated for 1 h to form a homogeneous ink.

Then 10 μL of ink was loaded onto a 1 cm^2 pretreated carbon paper (CP) and dried under infrared light for measurement.

Characterizations: X-ray powder diffraction (XRD) patterns were collected on a Shimadzu XRD-6100 diffractometer (Shimadzu, Japan) with a Cu Kα X-ray source. SEM images and corresponding EDX elemental mapping images were obtained from a GeminiSEM 300 field-emission scanning electron microscope (ZEISS, Germany) with an accelerating voltage of 5 kV. TEM and HRTEM images were performed on a Zeiss Libra 200FE transmission electron microscope at 200 kV. Raman spectra were obtained using a LabRAM HR Evolution Raman spectrometer. Electron paramagnetic resonance (EPR) measurements were conducted on a Bruker 500 spectrometer at 298 K. X-ray photoelectron spectroscopy (XPS) measurements were carried out on an ESCALAB 250Xi spectrometer equipped with monochromatized Al Kα radiation. Absorbance data were acquired on a Shimadzu UV-1800 UV-vis spectrophotometer. Ion chromatography (IC) data were obtained by using a ThermoFisher ICS 5000 plus IC. Gaseous products were detected by a Shimadzu GC-2014 gas chromatograph (GC) with thermal conductivity detector.

Electrochemical measurements: N_2 reduction experiments were carried out in a gastight H-type electrolytic cell separated by a Nafion 211 membrane under ambient conditions. The Nafion membrane was pretreated by heating in 3% H_2O_2 solution and 0.5 M H_2SO_4 at 80 ℃ for 1 h, respectively, and then immersed in deionized water for another 1 h. Electrochemical data were collected with a CHI760E electrochemical

workstation (Shanghai, Chenhua). In this work, OV-Ti_2O_3/CP, Ag/AgCl/saturated KCl, and graphite rod were used as the working electrode, reference electrode, and counter electrode, respectively. All potentials were converted to the reversible hydrogen electrode (RHE) through calibration (E (*vs* RHE) = E (*vs* Ag/AgCl) + 0.197 V + 0.059 × pH). Before NRR measurement, the HCl electrolyte was purged with N_2 for 30 min. For the NRR experiments, the chronoamperometry tests were performed in an N_2-saturated 0.1 M HCl solution (pH=1, 35 mL). During the electrolysis process, high-purity N_2 gas (99.999%) was continuously purged into the cathodic chamber at a flow rate of 20 mL min^{-1}.

Assembly of the Zn-N_2 battery and electrochemical test: The homemade rechargeable Zn-N_2 battery was assembled with OV-Ti_2O_3/CP (1 × 1 cm^2) electrode as the cathode and a polished Zn plate (1 × 1 cm^2) as the anode. A typical H-type cell containing 35 mL of cathode electrolyte (0.1 M HCl) and 35 mL of anode electrolyte (1 M KOH) is separated by a bipolar membrane (Nafion 211). N_2 gas was continuously bubbled into the catholyte during electrochemical testing. The discharge polarization curves with a scan rate of 2 mV s^{-1} and galvanostatic tests were performed on a CHI760E electrochemical workstation. The power density (P) of the Zn-N_2 battery was determined by $P = I \times V$, where I and V are the discharge current density and voltage, respectively.

The electrochemical reactions in Zn-N_2 battery are as follows:[1-3]

Cathode reaction: $N_2 + 6H_2O + 6e^- \rightarrow 2NH_3 + 6OH^-$

Anode reaction: $Zn + 2OH^- \rightarrow ZnO + H_2O + 2e^-$

Overall reaction: $3Zn + N_2 + 3H_2O \rightarrow 3ZnO + 2NH_3$

Determination of NH_3: The concentrations of NH_3 produced were detected by the indophenol blue method using a UV-vis spectrophotometer. Firstly, 2 mL of electrolyte was pipetted from the cathodic chamber and mixed with 2 mL of 1 M NaOH solution containing 5% $C_7H_6O_3$ and 5% $C_6H_5Na_3O_7 \cdot 2H_2O$. Then, 1 mL of 0.05 M NaClO and 0.2 mL of 1% $Na_2Fe(CN)_5NO \cdot 2H_2O$ were added to the above solution in turn. Finally, after standing for 120 min at room temperature, the absorbance measurements were performed in the range of 500 nm to 800 nm. The concentration-absorbance (at 655 nm) curves were calibrated by measuring a series of standard solutions with different NH_4Cl concentrations. The fitting curve of NH_3 ($y = 0.3848x + 0.036$, $R^2 = 0.999$) shows a good linear relationship between absorbance value and NH_4^+ concentration.

Determination of N_2H_4: The concentration of N_2H_4 was determined by Watt and Chrisp method. 5.99 g of p-$C_9H_{11}NO$, 30 mL of concentrated HCl, and 300 mL of C_2H_5OH were homogeneously mixed as a color reagent. Typically, 2 mL of electrolyte was removed from the cathodic chamber and mixed with 2 mL of the above-prepared color reagent. After standing for 10 min at room temperature, the UV-vis absorption spectra were collected at a wavelength of 455 nm. The fitting curve of N_2H_4 ($y = 0.389x + 0.041$, $R^2 = 0.999$) shows a good linear relationship between absorbance value with N_2H_4 concentration.

Calculations of NH_3 yield and Faradaic efficiency (FE):

NH_3 yield (V_{NH3}) was calculated using the following equation:

$$V_{NH3} = c(NH_3) \times V / (t \times m_{cat.}) \quad (1)$$

FE was calculated by the following equation:

$$FE_{NH3} = 3F \times c(NH_3) \times V / (17 \times Q) \times 100\% \quad (2)$$

where $c(NH_3)$ is the measured NH_3 concentration, V is the volume of the electrolyte in the cathodic chamber (35 mL), t is the electrolysis time (2 h), $m_{cat.}$ is the mass loading of the catalyst on CP (0.1 mg), F is the Faraday constant (96485 C mol^{-1}), and Q is the total charge passed through the electrode.

Calculation of FE for H_2:

FE for H_2 was calculated using the following equation:

$$FE_{H2} = 2F \times n(H_2) / Q \times 100\% \quad (3)$$

Calculations of electrochemical active surface area (ECSA) and turnover frequency (TOF): The ECSA of the electrode was determined by the electrochemical double-layer capacitance (C_{dl}). We tested the cyclic voltammetry curves of OV-Ti_2O_3 and pristine Ti_2O_3 at scanning rates of 20, 40, 60, 80, 100, 120, 140, and 160 mV s^{-1} to calculate the C_{dl} value. Moreover, the specific capacitance (C_s) for a flat surface is generally found to be in the range of 20~60 μF cm^{-2}. The ECSA was calculated by dividing the C_{dl} with the specific capacitance (C_s = 60 μF cm^{-2}) of flat electrodes in 0.1 M HCl.[4,5]

$$A_{ECSA} = C_{dI} / C_s \quad (4)$$

The TOF value of the electrocatalyst was calculated by the following equation:[6]

$$TOF = V_{NH3} \times m_{cat.} \times N_A / 17 \times \text{surface sites} \times A_{ECSA} \quad (5)$$

where N_A is Avogadro constant (6.023×10^{23} mol^{-1}). Since the exact nitrogen binding site is unknown, we conservatively estimate the number of active sites as the total number of surface sites. Surface Ti ions of Ti_2O_3 are considered to be catalytic active species (two Ti atoms and three O atoms with a volume of 313.5 $Å^3$).

Surface sites per real surface area:[7,8]

$$\text{Surface sites} = \left(\frac{\text{Atoms per unit cell}}{\text{Volume/unit cell}} \right)^{\frac{2}{3}} = \left(\frac{5 \text{ Atoms/unit cell}}{313.5 \text{ Å}^3\text{/unit cell}} \right)^{\frac{2}{3}} \quad (6)$$

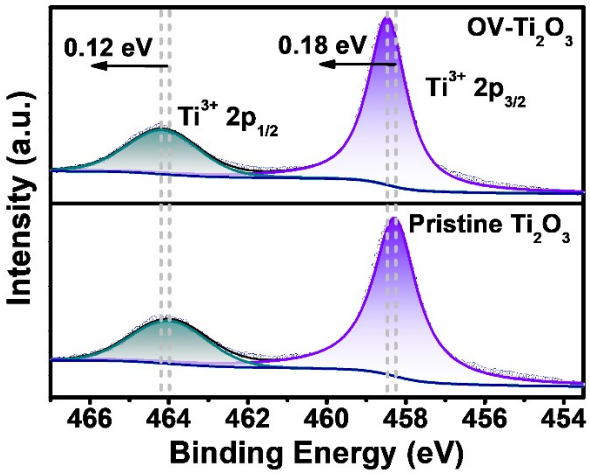

Fig. S1. XPS spectra of pristine Ti_2O_3 and OV-Ti_2O_3 in the Ti 2p region.

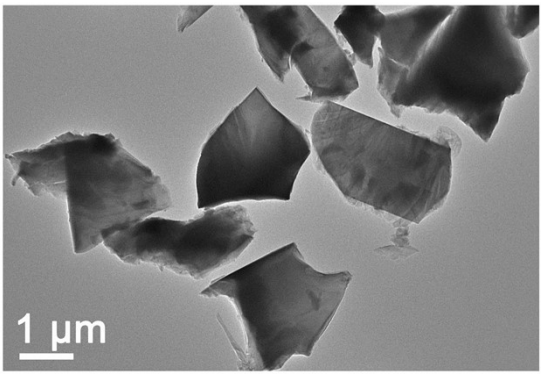

Fig. S2. TEM image of OV-Ti_2O_3.

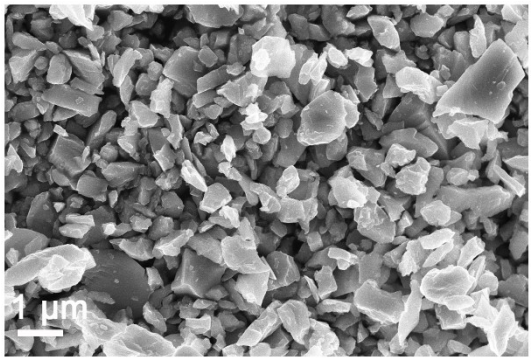

Fig. S3. SEM image of pristine Ti_2O_3.

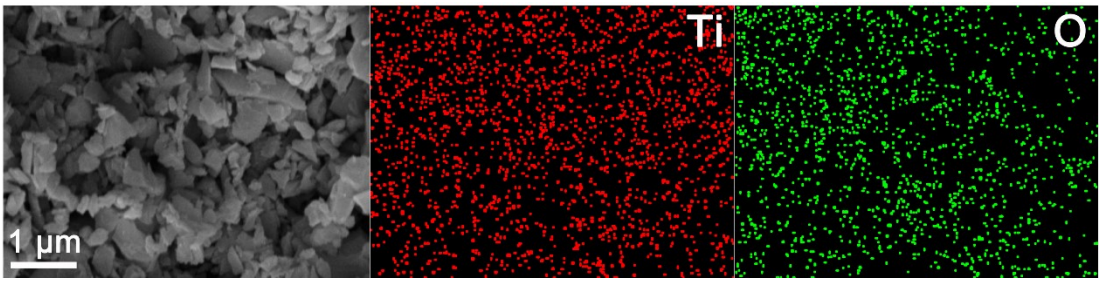

Fig. S4. SEM image and corresponding EDX elemental mapping images of OV-Ti_2O_3.

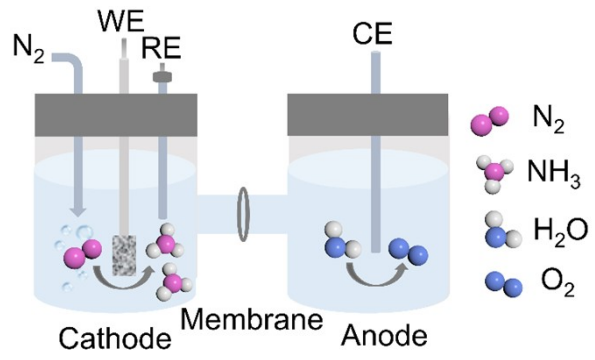

Cathode: $12H_2O + 2N_2 + 12e^- \rightarrow 4NH_3 + 12OH^-$
Anode: $12OH^- \rightarrow 3O_2 + 6H_2O + 12e^-$
Total: $6H_2O + 2N_2 \rightarrow 4NH_3 + 3O_2$

Fig. S5. Schematic illustration of the NRR process.

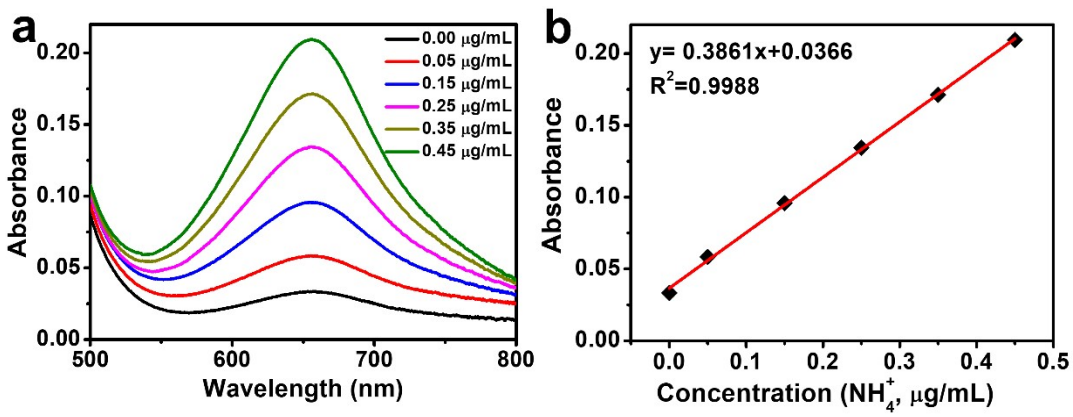

Fig. S6. (a) UV-vis absorption spectra of indophenol assays with NH_4^+ concentrations after incubated for 2 h at room temperature. (b) Calibration curve used for calculation of NH_4^+ concentrations.

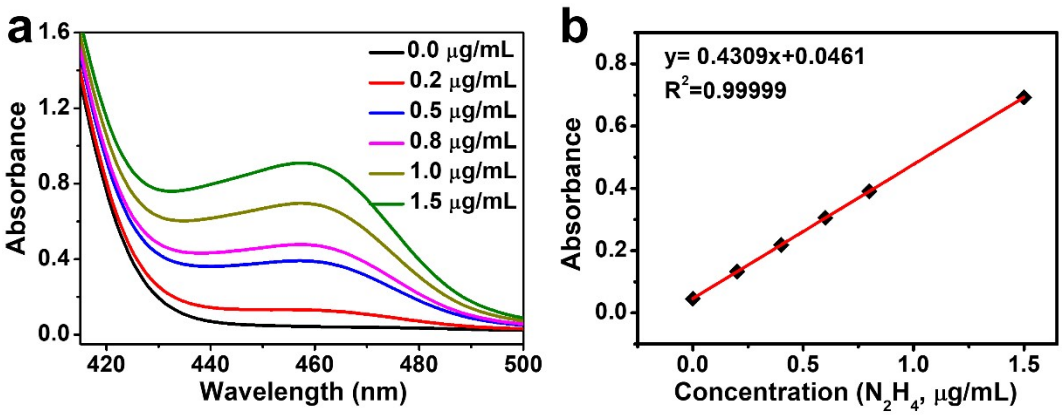

Fig. S7. (a) UV-vis absorption spectra of various N_2H_4 concentrations after incubated for 10 min at room temperature. (b) Calibration curve used for calculation of N_2H_4 concentrations.

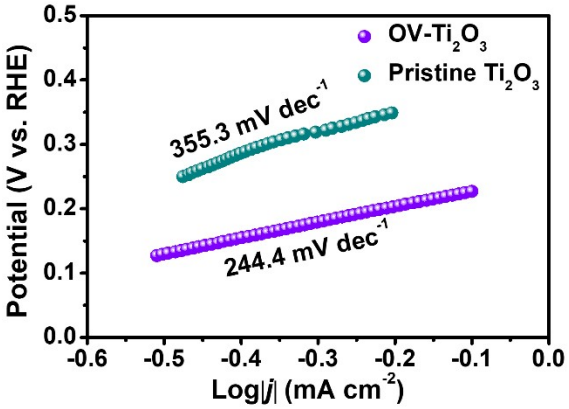

Fig. S8. Tafel plots of OV-Ti_2O_3 and pristine Ti_2O_3 catalysts for NRR.

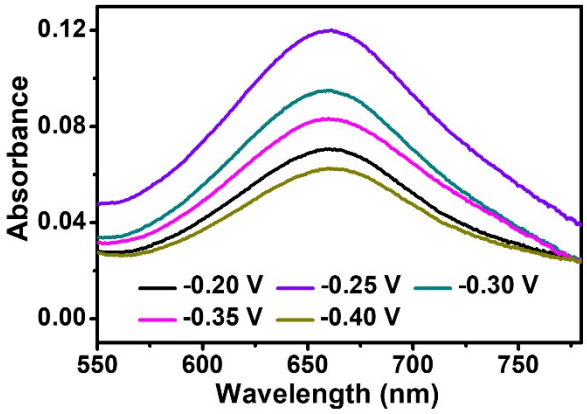

Fig. S9. UV-vis absorption spectra of the electrolytes stained with the indophenol indicator for the OV-Ti_2O_3 electrode at different potentials after NRR electrolysis for 2 h.

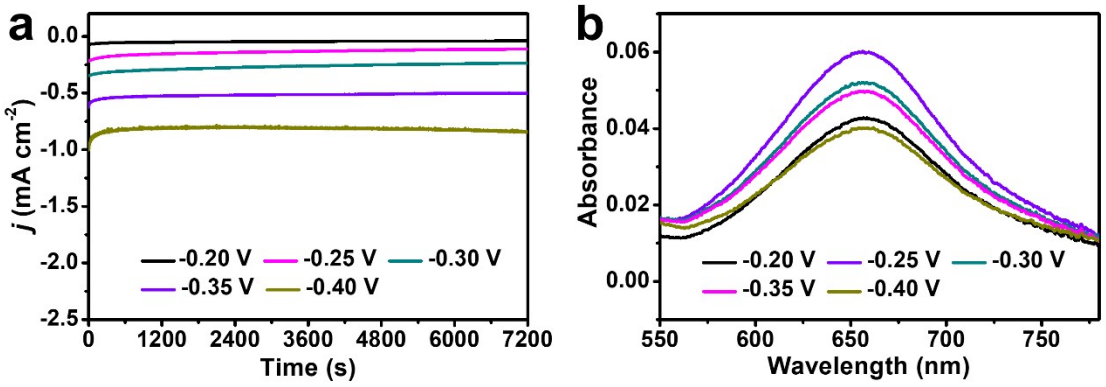

Fig. S10. (a) Chronoamperometry curves of pristine Ti_2O_3 at different potentials in N_2-saturated 0.1 M HCl solution. (b) Corresponding UV-vis absorption spectra of the electrolytes stained with the indophenol indicator after NRR electrolysis for 2 h.

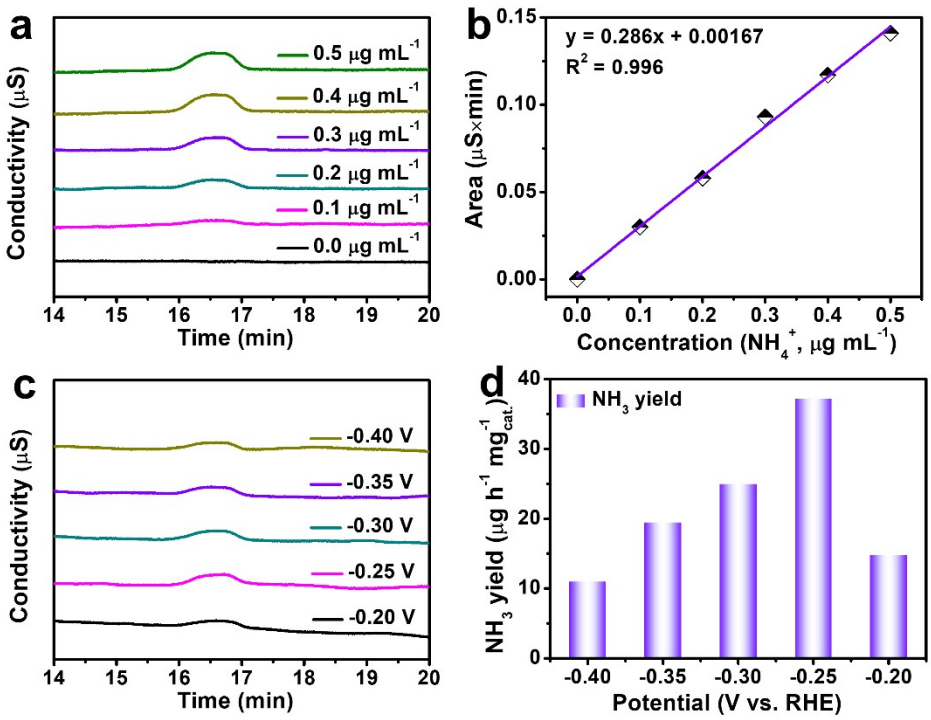

Fig. S11. (a) Ion chromatogram curves of the standard solution with NH_4^+ concentrations in 0.1 M HCl. (b) Calibration curve used for estimation of NH_4^+. (c) Ion chromatogram for the electrolytes at a series of potentials after electrolysis for 2 h. (d) NH_3 yields of OV-Ti_2O_3/CP at corresponding potentials.

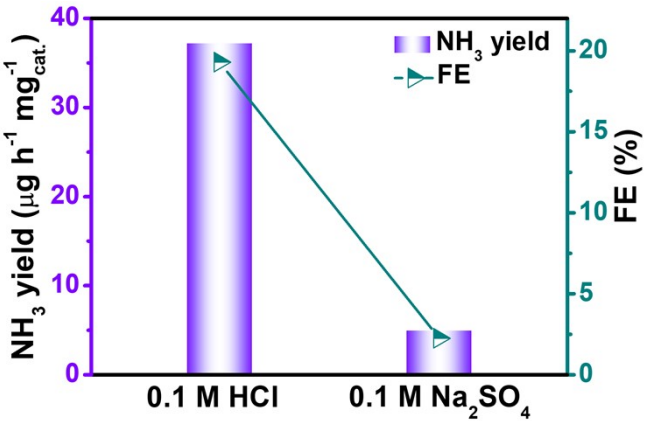

Fig. S12. NH_3 yields and FEs of OV-Ti_2O_3/CP at −0.25 V in 0.1 M HCl and 0.1 M Na_2SO_4.

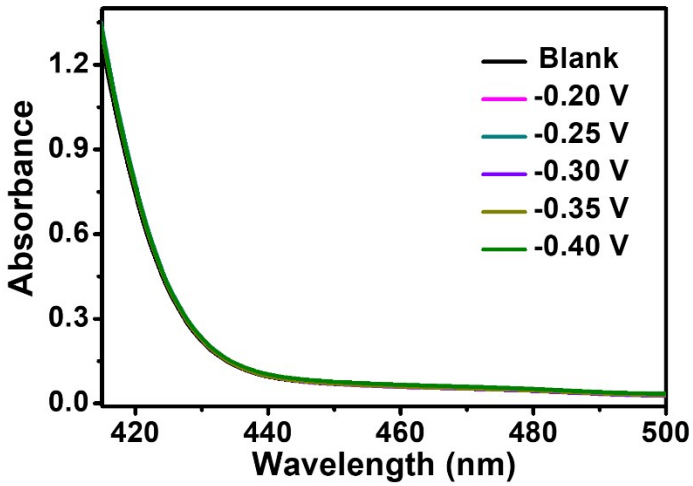

Fig. S13. UV-vis absorption spectra of the electrolytes detected by the method of Watt and Chrisp after 2 h electrolysis in N_2 atmosphere at a series of potentials.

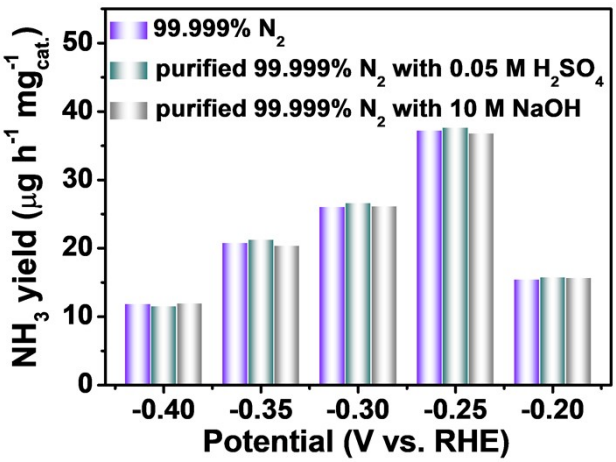

Fig. S14. Comparisons of the NH_3 yields at different applied potentials over OV-Ti_2O_3 using a feed gas of 99.999% N_2, and purified 99.999% N_2 with 0.05 M H_2SO_4 or 10 M NaOH.

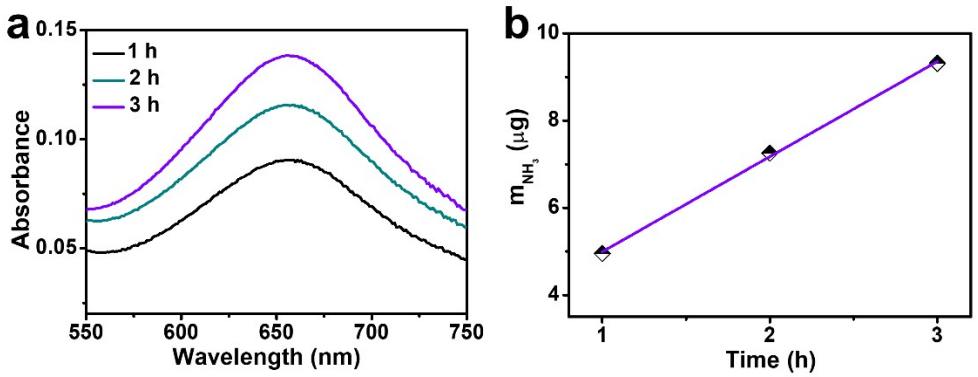

Fig. S15. (a) UV-vis spectra of the electrolytes with different electrolysis times at −0.25 V on the OV-Ti_2O_3 catalyst. (b) The mass of produced NH_3 *vs* electrolysis time at −0.25 V.

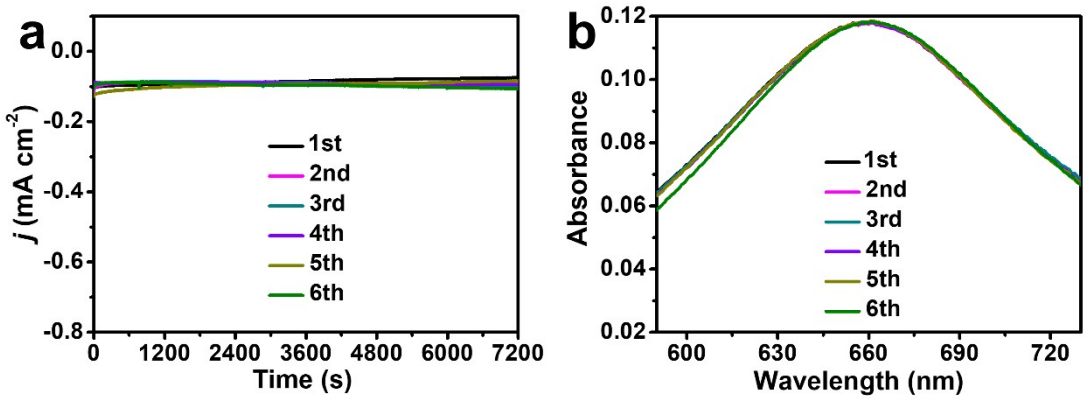

Fig. S16. (a) Chronoamperometry curves of OV-Ti_2O_3/CP under recycling tests for NRR at −0.25 V in 0.1 M HCl. (b) UV-vis absorption spectra of the electrolytes stained with indophenol indicator after NRR electrolysis.

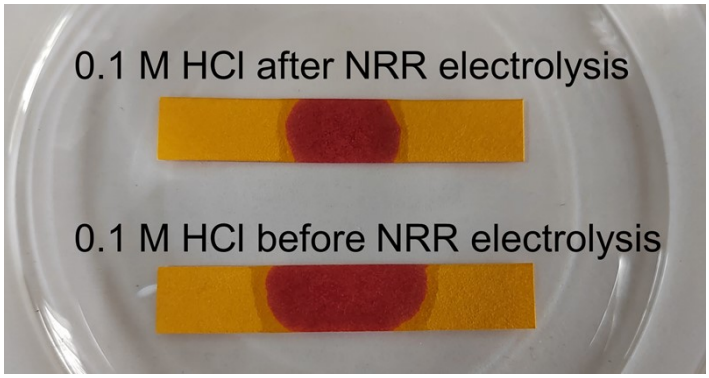

Fig. S17. Photographs of pH test strips in 0.1 M HCl before and after 12-h electrolysis.

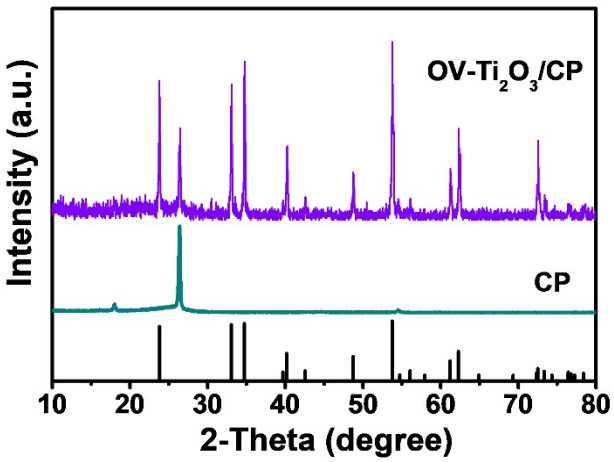

Fig. S18. XRD pattern for OV-Ti_2O_3/CP after long-term NRR electrolysis.

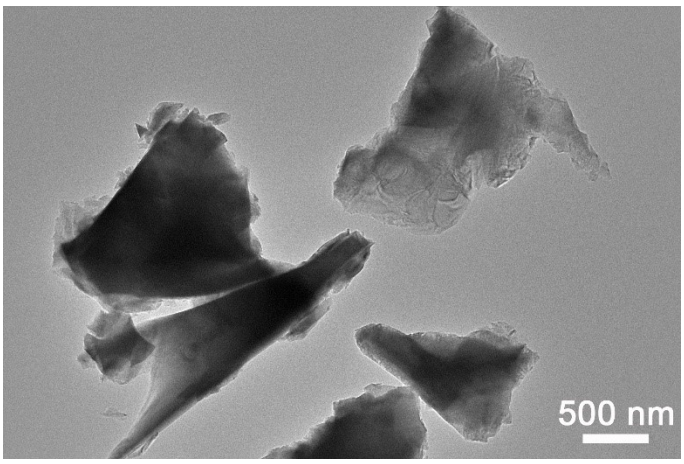

Fig. S19. TEM image for OV-Ti_2O_3/CP after long-term NRR electrolysis.

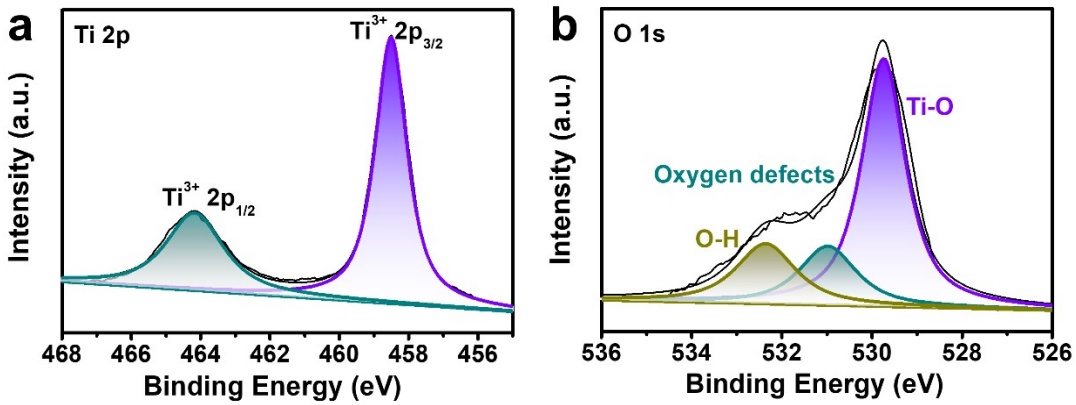

Fig. S20. XPS spectra of OV-Ti_2O_3/CP after long-term NRR electrolysis.

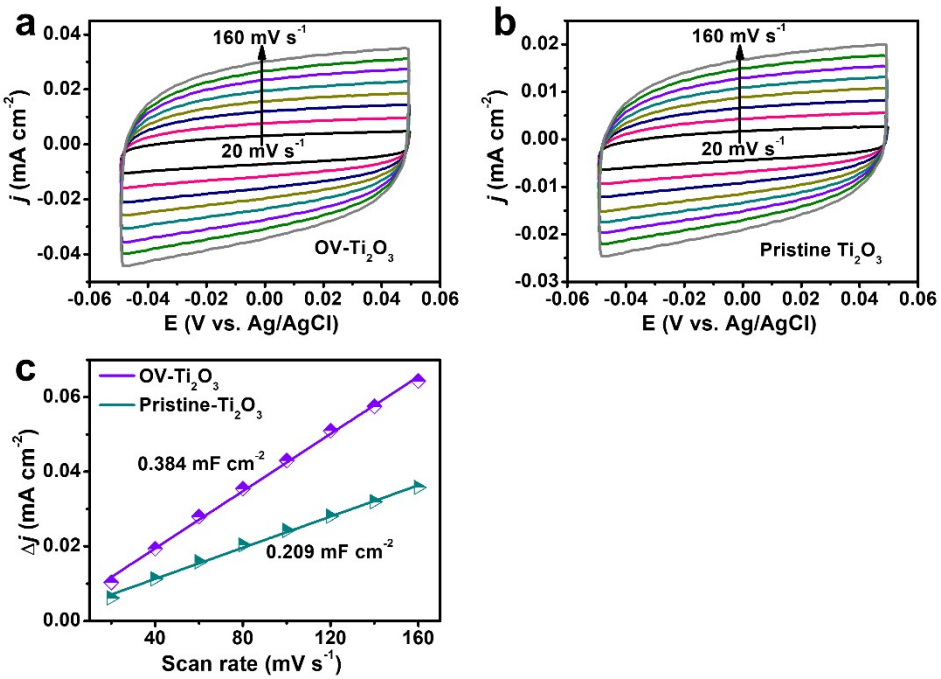

Fig. S21. Cyclic voltammetry curves of (a) OV-Ti_2O_3/CP, and (b) pristine Ti_2O_3/CP with various scan rates (20-160 mV s^{-1}) in the region of −0.05 to 0.05 V *vs* Ag/AgCl. (c) The corresponding double-layer capacitance (C_{dl}) of OV-Ti_2O_3/CP and pristine Ti_2O_3/CP.

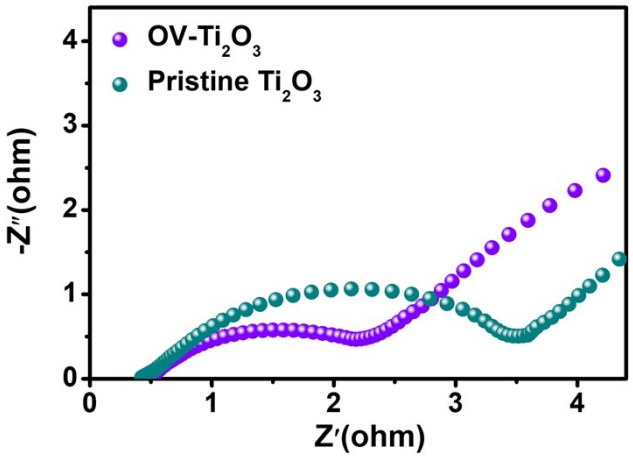

Fig. S22. Nyquist plots of OV-Ti_2O_3 and pristine Ti_2O_3.

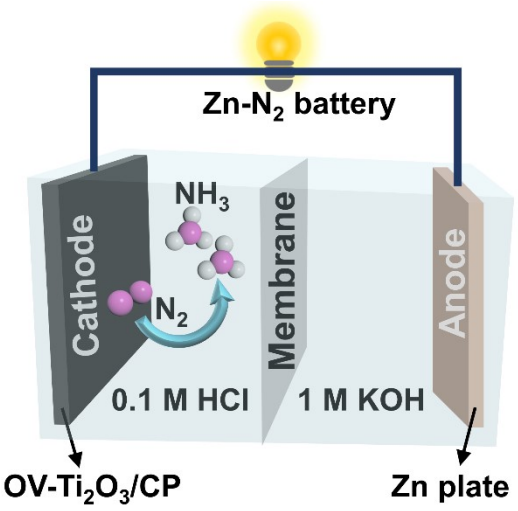

Fig. S23. Schematic illustration of Zn-N_2 battery.

Table S1. Comparison of the electrocatalytic NRR performances of OV-Ti_2O_3 with other reported Ti-based catalysts under ambient conditions.

Catalyst	Electrolyte	NH_3 yield	FE (%)	Ref.
OV-Ti_2O_3	0.1 M HCl	37.24 μg h^{-1} $mg_{cat.}^{-1}$	19.29	This work
Ti_2O_3	0.1 M HCl	26.01 μg h^{-1} $mg_{cat.}^{-1}$	9.16	9
$TiO_2(V_O)$	0.1 M HCl	3.0 μg h^{-1} $mg_{cat.}^{-1}$	6.5	10
OV-TiO_2 nanosheets	0.005 M H_2SO_4	35.6 μg h^{-1} $mg_{cat.}^{-1}$	5.3	11
Ru/TiO_2-V_O	0.1 M KOH	2.11 μg h^{-1} cm^{-2}	0.72	12
Pd-Co/TiO_2-V_O	0.1 M KOH	4.11 μg h^{-1} cm^{-2}	2.83	13
Ag@TiO_2	0.1 M Na_2SO_4	14.88 μg h^{-1} $mg_{cat.}^{-1}$	6.2	14
B-doped TiO_2	0.1 M Na_2SO_4	14.4 μg h^{-1} $mg_{cat.}^{-1}$	3.4	15
Mn-doped TiO_2	0.1 M Na_2SO_4	20.05 μg h^{-1} $mg_{cat.}^{-1}$	11.93	16
Pd-doped TiO_2	0.1 M Na_2SO_4	17.4 μg h^{-1} $mg_{cat.}^{-1}$	12.7	17
TiO_2/JE-CMTs	0.1 M Na_2SO_4	20.03 μg h^{-1} $mg_{cat.}^{-1}$	10.76	18
V-doped TiO_2	0.5 M $LiClO_4$	17.73 μg h^{-1} $mg_{cat.}^{-1}$	15.3	19
TiO_2/Ti	0.1 M Na_2SO_4	5.6 μg h^{-1} $mg_{cat.}^{-1}$	2.5	20
Ti^{3+}–TiO_{2-x}/TM	0.1 M Na_2SO_4	3.51×10^{-10} mol s^{-1} cm^{-2}	14.62	21
d-TiO_2/TM	0.1 M HCl	7.58 μg h^{-1} $mg_{cat.}^{-1}$	9.17	22
C-Ti_xO_y/C	0.1 M Li_2SO_4	14.8 μg h^{-1} $mg_{cat.}^{-1}$	17.8	23
TiC/C NF	0.1 M HCl	14.1 μg h^{-1} $mg_{cat.}^{-1}$	5.8	24
Zr-doped TiO_2	1.0 M KOH	8.9 μg h^{-1} cm^{-2}	17.3	25
La-doped TiO_2	0.1 M $LiClO_4$	23.06 μg h^{-1} $mg_{cat.}^{-1}$	14.54	26

Table S2. Comparison of NH_3 yield and power density of our battery with the reported Zn-N_2 battery systems.

Battery systems	Catalysts	Power density	NH_3 yield	Ref.
Zn-N_2	OV-Ti_2O_3	1.02 mW cm^{-2}	4.3 μg h^{-1} $mg_{cat.}^{-1}$	This work
Zn-N_2	CoPi/HSNPC	0.33 mW cm^{-2}	11.58 μg h^{-1} $mg_{cat.}^{-1}$	1
Zn-N_2	CoPi/NPCS	0.49 mW cm^{-2}	14.7 μg h^{-1} $mg_{cat.}^{-1}$	27
Zn-N_2	nano-Cu	0.0101 mW cm^{-2}	0.125 μg h^{-1} cm^{-2}	2
Zn-N_2	NbS_2 nanosheets	0.31 mW cm^{-2}	/	28
Zn-N_2	VN@NSC-900	0.01642 mW cm^{-2}	0.172 μg h^{-1} cm^{-2}	3
Zn-N_2	$Fe_{1.0}$HTNs	0.02765 mW cm^{-2}	0.137 μg h^{-1} cm^{-2}	29
Zn-N_2	Vs-$FePS_3$ NSs	2.6 mW cm^{-2}	/	30

References

1 J. T. Ren, L. Chen, Y. Liu and Z. Y. Yuan, Hollow cobalt phosphate microspheres for sustainable electrochemical ammonia production through rechargeable Zn-N_2 batteries, *J. Mater. Chem. A*, 2021, **9**, 11370−11380.

2 C. Du, Y. Gao, J. Wang and W. Chen, Achieving 59% faradaic efficiency of the N_2 electroreduction reaction in an aqueous Zn-N_2 battery by facilely regulating the surface mass transport on metallic copper, *Chem. Commun.*, 2019, **55**, 12801−12804.

3 X. W. Lv, Y. Liu, Y. S. Wang, X. L. Liu and Z. Y. Yuan, Encapsulating vanadium nitride nanodots into N,S-codoped graphitized carbon for synergistic electrocatalytic nitrogen reduction and aqueous Zn-N_2 battery, *Appl. Catal. B: Environ.*, 2021, **280**, 119434.

4 T. Xu, D. Ma, T. Li, L. Yue, Y. Luo, S. Lu, X. Shi, A. M. Asiri, C. Yang and X. Sun, Enhanced electrocatalytic N_2-to-NH_3 fixation by ZrS_2 nanofibers with a sulfur vacancy, *Chem. Commun.*, 2020, **56**, 14031−14034.

5 D. Liu, X. Li, S. Chen, H. Yan, C. Wang, C. Wu, Y. A. Haleem, S. Duan, J. Lu, B. Ge, P. M. Ajayan, Y. Luo, J. Jiang and L. Song, Atomically dispersed platinum supported on curved carbon supports for efficient electrocatalytic hydrogen evolution, *Nat. Energy*, 2019, **4**, 512−518.

6 Y. Yang, L. Zhang, Z. Hu, Y. Zheng, C. Tang, P. Chen, R. Wang, K. Qiu, J. Mao, T. Ling and S. Z. Qiao, The crucial role of charge accumulation and spin

polarization in activating carbon-based catalysts for electrocatalytic nitrogen reduction, *Angew. Chem. Int. Ed.*, 2020, **59**, 4525−4531.

7 H. Fei, T. Guo, Y. Xin, L. Wang, R. Liu, D. Wang, F. Liu and Z. Wu, Sulfur vacancy engineering of MoS_2 via phosphorus incorporation for improved electrocatalytic N_2 reduction to NH_3, *Appl. Catal. B: Environ.*, 2022, **300**, 120733.

8 W. Xu, G. Fan, J. Chen, J. Li, L. Zhang, S. Zhu, X. Su, F. Cheng and J. Chen, Nanoporous palladium hydride for electrocatalytic N_2 reduction under ambient conditions, *Angew. Chem. Int. Ed.*, 2020, **59**, 3511−3516.

9 H. Chen, J. Liang, L. Li, B. Zheng, Z. Feng, Z. Xu, Y. Luo, Q. Liu, X. Shi, Y. Liu, S. Gao, A. M. Asiri, Y. Wang, Q. Kong and X. Sun, Ti_2O_3 nanoparticles with Ti^{3+} sites toward efficient NH_3 electrosynthesis under ambient conditions, *ACS Appl. Mater. Interfaces*, 2021, **13**, 41715−41722.

10 Z. Han, C. Choi, S. Hong, T.-S. Wu, Y.-L. Soo, Y. Jung, J. Qiu and Z. Sun, Activated TiO_2 with tuned vacancy for efficient electrochemical nitrogen reduction, *Appl. Catal. B: Environ.*, 2019, **257**, 117896.

11 C. Fang, T. Bi, X. Xu, N. Yu, Z. Cui, R. Jiang and B. Geng, Oxygen vacancy-enhanced electrocatalytic performances of TiO_2 nanosheets toward N_2 reduction reaction, *Adv. Mater. Interfaces*, 2019, **6**, 1901034.

12 S. Cheng, Y. J. Gao, Y. L. Yan, X. Gao, S. H. Zhang, G. L. Zhuang, S. W. Deng, Z. Z. Wei, X. Zhong and J. G. Wang, Oxygen vacancy enhancing mechanism of nitrogen reduction reaction property in Ru/TiO_2, *J. Energy Chem.*, 2019, **39**,

144−151.

13 S. Zhang, W. Wang, Y. Gao, S. Deng, L. Ding, H. Zhuo, Z. Bao, W. Ji, C. Qiu and J. Wang, Pd-Co alloy supported on TiO_2 with oxygen vacancies for efficient N_2 and O_2 electrocatalytic reduction, *Appl. Surf. Sci.*, 2021, **567**, 150680.

14 X. Li, Y. Cao, T. Xu, Y. Luo, T. Li, H. Zhao, S. Lu, X. Shi, A. M. Asiri, J. Hu, Q. Liu and X. Sun, Ag@TiO_2 as an efficient electrocatalyst for N_2 fixation to NH_3 under ambient conditions, *ChemistrySelect*, 2021, **6**, 5271−5274.

15 Y. Wang, K. Jia, Q. Pan, Y. Xu, Q. Liu, G. Cui, X. Guo and X. Sun, Boron-doped TiO_2 for efficient electrocatalytic N_2 fixation to NH_3 at ambient conditions, *ACS Sustainable Chem. Eng.*, 2019, **7**, 117−122.

16 H. Chen, T. Wu, X. Li, S. Lu, F. Zhang, Y. Wang, H. Zhao, Q. Liu, Y. Luo, A. M. Asiri, Z. Feng, Y. Zhang and X. Sun, Modulating oxygen vacancies of TiO_2 nanospheres by Mn-doping to boost electrocatalytic N_2 reduction, *ACS Sustainable Chem. Eng.*, 2021, **9**, 1512−1517.

17 H. J. Chen, G. R. Deng, Z. S. Feng, Z. Q. Xu, M. Y. Yang, Y. Huang, Q. Peng, T. Li and Y. Wang, Enhanced electrocatalytic performance of TiO_2 nanoparticles by Pd doping toward ammonia synthesis under ambient conditions, *Chem. Commun.*, 2022, **58**, 3214−3217.

18 H. Chen, J. Liang, K. Dong, L. Yue, T. Li, Y. Luo, Z. Feng, N. Li, M. S. Hamdy, A. A. Alshehri, Y. Wang, X. Sun and Q. Liu, Ambient electrochemical N_2-to-NH_3 conversion catalyzed by TiO_2 decorated juncus effusus-derived carbon

microtubes, *Inorg. Chem. Front.*, 2022, **9**, 1514−1519.

19 T. Wu, W. Kong, Y. Zhang, Z. Xing, J. Zhao, T. Wang, X. Shi, Y. Luo and X. Sun, Greatly enhanced electrocatalytic N_2 reduction on TiO_2 via V doping, *Small Methods*, 2019, **3**, 1900356.

20 R. Zhang, X. Ren, X. Shi, F. Xie, B. Zheng, X. Guo and X. Sun, Enabling effective electrocatalytic N_2 conversion to NH_3 by the TiO_2 nanosheets array under ambient conditions, *ACS Appl. Mater. Interfaces*, 2018, **10**, 28251−28255.

21 B. Li, X. Zhu, J. Wang, R. Xing, Q. Liu, X. Shi, Y. Luo, S. Liu, X. Niu and X. Sun, Ti^{3+} self-doped TiO_{2-x} nanowires for efficient electrocatalytic N_2 reduction to NH_3, *Chem. Commun.*, 2020, **56**, 1074−1077.

22 L. Yang, T. Wu, R. Zhang, H. Zhou, L. Xia, X. Shi, H. Zheng, Y. Zhang and X. Sun, Insights into defective TiO_2 in electrocatalytic N_2 reduction: combining theoretical and experimental studies, *Nanoscale*, 2019, **11**, 1555−1562.

23 Q. Qin, Y. Zhao, M. Schmallegger, T. Heil, J. Schmidt, R. Walczak, G. Gescheidt-Demner, H. Jiao and M. Oschatz, Enhanced electrocatalytic N_2 reduction via partial anion substitution in titanium oxide-carbon composites, *Angew. Chem. Int. Ed.*, 2019, **58**, 13101−13106.

24 G. Yu, H. Guo, W. Kong, T. Wang, Y. Luo, X. Shi, A. M. Asiri, T. Li and X. Sun, Electrospun TiC/C nanofibers for ambient electrocatalytic N_2 reduction, *J. Mater. Chem. A*, 2019, **7**, 19657−19661.

25 N. Cao, Z. Chen, K. Zang, J. Xu, J. Zhong, J. Luo, X. Xu and G. Zheng, Doping

strain induced bi-Ti^{3+} pairs for efficient N_2 activation and electrocatalytic fixation, *Nat. Commun.*, 2019, **10**, 2877.

26 L. Li, H. Chen, L. Li, B. Li, Q. Wu, C. Cui, B. Deng, Y. Luo, Q. Liu, T. Li, F. Zhang, A. M. Asiri, Z. S. Feng, Y. Wang and X. Sun, La-doped TiO_2 nanorods toward boosted electrocatalytic N_2-to-NH_3 conversion at ambient conditions, *Chin. J. Catal.*, 2021, **42**, 1755−1762.

27 J. T. Ren, L. Chen, H. Y. Wang and Z. Y. Yuan, Aqueous rechargeable Zn-N_2 battery assembled by bifunctional cobalt phosphate nanocrystals-loaded carbon nanosheets for simultaneous NH_3 production and power generation, *ACS Appl. Mater. Interfaces*, 2021, **13**, 12106−12117.

28 H. Wang, J. Si, T. Zhang, Y. Li, B. Yang, Z. Li, J. Chen, Z. Wen, C. Yuan, L. Lei and Y. Hou, Exfoliated metallic niobium disulfate nanosheets for enhanced electrochemical ammonia synthesis and Zn-N_2 battery, *Appl. Catal. B: Environ.*, 2020, **270**, 118892.

29 X. W. Lv, X. L. Liu, L. J. Gao, Y. P. Liu and Z. Y. Yuan, Iron-doped titanium dioxide hollow nanospheres for efficient nitrogen fixation and Zn-N_2 aqueous batteries, *J. Mater. Chem. A*, 2021, **9**, 4026−4035.

30 H. Wang, Z. Li, Y. Li, B. Yang, J. Chen, L. Lei, S. Wang and Y. Hou, An exfoliated iron phosphorus trisulfide nanosheet with rich sulfur vacancy for efficient dinitrogen fixation and Zn-N_2 battery, *Nano Energy*, 2021, **81**, 105613.